

# Revealing Grain Boundaries and Defect Formation in Nanocrystal Superlattices by Nanodiffraction

Nastasia Mukharamova, Dmitry Lapkin, Ivan A. Zaluzhnyy, Alexander André, Sergey Lazarev, Young Yong Kim, Michael Sprung, Ruslan P. Kurta, Frank Schreiber, Ivan A. Vartanyants,\* and Marcus Scheele\*

X-ray nanodiffraction is applied to study the formation and correlation of domain boundaries in mesocrystalline superlattices of PbS nanocrystals with face-centered cubic structure. Each domain of the superlattice can be described with one of two mesocrystalline polymorphs with different orientational orders. Close to a grain boundary, the lattice constant decreases and the superlattice undergoes an out-of-plane rotation, while the orientation of the nanocrystals with respect to the superlattice remains unchanged. These findings are explained with the release of stress on the expense of specific nanocrystal–substrate interactions. The fact that correlations between adjacent nanocrystals are found to survive the structural changes at most grain boundaries implies that the key to nanocrystal superlattices with macroscopic domain sizes are strengthened interactions with the substrate.

## 1. Introduction

Superlattices of inorganic nanocrystals (NCs) are often viewed as large-scale analogs to crystalline lattices of atoms.<sup>[1,2]</sup> In line with this analogy, homogenous NC ensembles crystallize in common close-packed structures, such as face-centered cubic (fcc), body-centered cubic (bcc), body-centered tetragonal (bct), or hexagonal close-packed arrangements.<sup>[3–7]</sup> Such ordered superlattices are held together by directional forces between


adjacent NCs, which span a wide spectrum from weak van der Waals interactions to ionic and covalent bonds.<sup>[3,8,9]</sup> Anisotropic, facet-specific interactions invoke orientational order of NCs into mesocrystalline assemblies with a global angular correlation between the superlattice and the atomic lattices of its NCs.<sup>[10,11]</sup> When these interactions are weakened, e.g., due to stress induced by polydisperse NCs or by uniaxial strain applied to the superlattice, defects occur which lead to the manifestation of grain boundaries and polycrystallinity.<sup>[12,13]</sup> Since the surface of NCs consists of different facets with different polarities, ligand binding motifs, and strengths, defects in the superlat-

tice form predominantly along the direction with the weakest binding strength.

One of the most common defects in NC superlattices are twin boundaries, which have previously been studied by electron microscopy, electron diffraction, or small-angle X-ray scattering.<sup>[5,12,14–16]</sup> Furthermore, NC superlattices are prone to other defects such as point, line, planar, or volume defects.<sup>[12,14,17]</sup> A detailed understanding of their origin is expected to improve the design of NC superlattices with tailored mechanical, electric, and optical properties.<sup>[18]</sup> Equally important is their

N. Mukharamova, D. Lapkin, Dr. I. A. Zaluzhnyy,<sup>[†]</sup> Dr. S. Lazarev, Dr. Y. Y. Kim, Dr. M. Sprung, Prof. I. A. Vartanyants  
Deutsches Elektronen-Synchrotron DESY  
Notkestrasse 85, D-22607 Hamburg, Germany  
E-mail: ivan.vartanyants@desy.de

Dr. I. A. Zaluzhnyy, Prof. I. A. Vartanyants  
National Research Nuclear University MEPhI  
(Moscow Engineering Physics Institute)  
Kashirskoe shosse 31, 115409 Moscow, Russia

 The ORCID identification number(s) for the author(s) of this article can be found under <https://doi.org/10.1002/smll.201904954>.

© 2019 The Authors. Published by WILEY-VCH Verlag GmbH & Co. KGaA, Weinheim. This is an open access article under the terms of the Creative Commons Attribution-NonCommercial-NoDerivs License, which permits use and distribution in any medium, provided the original work is properly cited, the use is non-commercial and no modifications or adaptations are made.

<sup>[†]</sup>Present address: Department of Physics, University of California San Diego, La Jolla, Ca 92093, USA

DOI: 10.1002/smll.201904954

Dr. A. André, Dr. M. Scheele  
Institute of Physical and Theoretical Chemistry  
University of Tübingen  
Auf der Morgenstelle 18, 72076 Tübingen, Germany  
E-mail: marcus.scheele@uni-tuebingen.de

Dr. S. Lazarev  
Tomsk Open Laboratory for Material Inspection (TOLMI)  
National Research Tomsk Polytechnic University (TPU)  
pr. Lenina 30, 634050 Tomsk, Russia

Dr. R. P. Kurta  
European XFEL GmbH  
Holzkoppel 4, D-22869 Schenefeld, Germany

Prof. F. Schreiber  
Institute of Applied Physics  
University of Tübingen  
Auf der Morgenstelle 10, 72076 Tübingen, Germany

Prof. F. Schreiber, Dr. M. Scheele  
Center for Light-Matter Interaction  
Sensors & Analytics LISA+  
University of Tübingen  
Auf der Morgenstelle 15, 72076 Tübingen, Germany

role as a model for grain boundary formation in general and the nature of the spatial transition between these. Specifically, in view of the previously found correlations between the orientation of individual NCs and the superlattice, are these correlations preserved through grain boundaries, and, if so, in which way?<sup>[7,8,11]</sup> How does the structure change close to the grain boundaries? Addressing these fundamental questions on structure formation would also shed light on the intriguing question to which degree superlattices of NCs serve as a model for atomic crystalline systems and where this analogy ends.<sup>[2]</sup>

Here, we use angular X-ray cross-correlation analysis (XCCA) in conjunction with a nanofocused X-ray beam to reveal the structure and orientational order in superlattices of PbS NCs linked by oleic acid molecules near grain boundaries.<sup>[11,19–21]</sup> We find that the superlattice forms an fcc structure and that the lattice constant is homogeneous within a single-crystalline domain. Close to the edges, it decreases by 5–10%, which is often accompanied by a rotation of the superlattice. We determine two different angular correlations between the superlattice and the atomic lattices of the NCs. This highlights the greater flexibility of the interparticle attractions in fcc superlattices of NCs compared to bcc assemblies which exhibit mostly a single angular correlation.<sup>[7,11,16]</sup> Our results enable a deepened understanding of the origin of defects in NC superlattices, highlight the role of orientational order in this respect, and serve to tailor the mechanical properties of NC-based materials.

## 2. Results

### 2.1. Definition of Crystalline Domains and Their Orientation

The X-ray scattering experiments were performed at the Coherence Beamline P10 of the PETRA III synchrotron facility (see the Experimental Section in the Supporting Information for details). The PbS mesocrystal sample was scanned with 250 nm resolution, and small angle as well as wide angle X-ray scattering (SAXS and WAXS) were simultaneously measured. Figure 1a,b displays an X-ray scanning image of a polycrystalline superlattice of PbS NCs, utilizing the positions of superlattice (SL) peaks at  $q^{\text{SL}} = 0.083 \text{ \AA}^{-1}$  (Figure 1a) and of the atomic lattice (AL) peaks at  $q^{\text{AL}} = 2.12 \text{ \AA}^{-1}$  (Figure 1b) (see the Supporting Information for more details). Throughout this paper, all reflections, planes and crystallographic directions referring to superlattice of the PbS NCs will be denoted with the index “sl” and from the atomic lattice with the index “AL”. Spatial positions of the sample with the same angular orientation of peaks in SAXS (Figure 1d–h) and WAXS (Figure 1i–m) diffraction patterns are indicated by the same color and specified by individual diffraction patterns. Gray color stands for areas with scattering signal but without a well-defined angular orientation (see the Supporting Information for details). A comparison with an optical microscopy image of the sample (Figure 1c) shows very good resemblance between the spatially distributed scattering intensity and the real-space image.

From the color code, the domain structure of the superlattice of NCs with single-crystalline grains and areas of 50–100  $\mu\text{m}^2$  is easily visible. We determine five typical patterns for both SAXS

(Figure 1d–h) and WAXS (Figure 1i–m) which are sufficient to categorize all SAXS and WAXS patterns.

The integrated SAXS patterns (Figure 1d–h) contain many orders of SL peaks and can be indexed according to an fcc structure with the cell parameter  $a^{\text{SL}} = 150 \text{ \AA}$  (see also Figures S4 and S5 and Table S1 in the Supporting Information for further details). The nearest-neighbor distance in this case is 106  $\text{\AA}$ . This value is consistent with the NC size of  $68 \pm 5 \text{ \AA}$  measured by optical spectroscopy and the length of oleic acid of 19  $\text{\AA}$  (on each NC) as detailed in Figures S2 and S3 (Supporting Information). The narrow size of all diffraction spots indicates that these parameters are uniform over each domain, and we note that we find excellent agreement with these  $q$ -values in all domains of the sample (see the Supporting Information). For the SL, we observe either the  $[001]_{\text{SL}}$  or the  $[110]_{\text{SL}}$  direction along the surface normal as the two dominant orientations. In the rare case of the orange-colored SAXS domain, the  $[301]_{\text{SL}}$  direction is perpendicular to the surface.

At wide angles, we observe X-ray scattering from the  $\{111\}$  and  $\{200\}$  planes of the AL with rock-salt structure at  $q_{111}^{\text{AL}} = 1.84 \text{ \AA}^{-1}$  and  $q_{200}^{\text{AL}} = 2.12 \text{ \AA}^{-1}$ , respectively, which allows us to unambiguously determine the orientation of the AL in each WAXS domain. Specifically, in the yellow, green, and orange WAXS domains (Figure 1i–k), we detect  $111_{\text{AL}}$  and  $200_{\text{AL}}$  peaks, while in the purple WAXS domain (Figure 1m), we find two  $200_{\text{AL}}$  peaks, and a single  $200_{\text{AL}}$  peak in the red WAXS domain (Figure 1l) (see also Figure S4 in the Supporting Information). These patterns correspond to two dominant orientations of the AL: the yellow, green, and orange WAXS domains exhibit the  $[110]_{\text{AL}}$  direction perpendicular to the sample surface, while in the red and purple WAXS domains, the  $[100]_{\text{AL}}$  direction is orthogonal to the sample surface.

Three domains, namely the red, orange, and purple, exhibit nearly identical spatial dimensions in SAXS and WAXS. By contrast, the yellow WAXS domain coincides with two SAXS domains – green and yellow. From here on, we will focus on a discussion of the SAXS domains.

### 2.2. Determination of the NC Orientation in the SL

To determine correlations between the superlattice structure and the orientation of its NCs, we apply an angular XCCA approach (see the Supporting Information for details).<sup>[20,21]</sup> We calculate the two-point angular cross-correlation functions (CCF) for all five domains according to

$$C(q_1, q_2, \Delta) = \langle I(q_1, \varphi) I(q_2, \varphi + \Delta) \rangle_{\varphi} \quad (1)$$

where  $I(q, \varphi)$  is the intensity at  $(q, \varphi)$  point of the diffraction pattern and  $\varphi$  is the angular coordinate around a diffraction ring. We correlate the intensities of the momentum transfer  $q_1 = q_{200}^{\text{SL}} = 0.83 \text{ \AA}^{-1}$ ,  $q_2 = q_{200}^{\text{AL}} = 2.12 \text{ \AA}^{-1}$  for the yellow and red domains, and  $q_1 = q_{311}^{\text{SL}} = 0.143 \text{ \AA}^{-1}$ ,  $q_2 = q_{200}^{\text{AL}} = 2.12 \text{ \AA}^{-1}$  for the green, purple, and orange domains.

In Figure 2, we determine the relative orientations of the NCs in the sample. The figure is structured as follows: the first row (Figure 2a–e) shows the CCFs. The second row (Figure 2f–j) contains the corresponding WAXS and SAXS patterns integrated

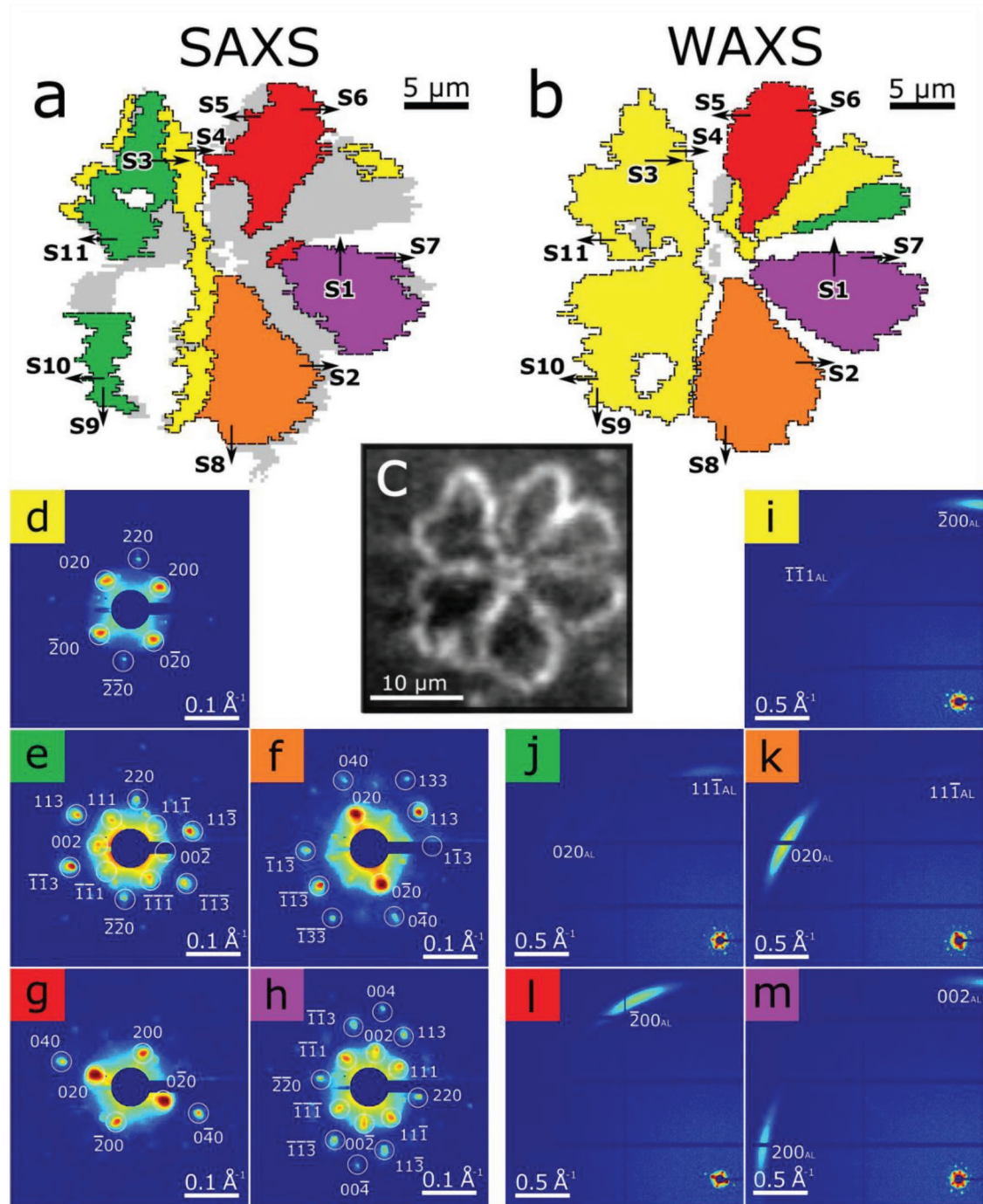


**Figure 1.** Spatially resolved maps of a mesocrystalline superlattice of PbS NCs, showing the domain structure. Each color corresponds to different orientations of a) the peaks at  $q^{\text{SL}} = 0.083 \text{ \AA}^{-1}$  for the SL and b) the peaks at  $q^{\text{AL}} = 2.12 \text{ \AA}^{-1}$  for the AL. Gray color stands for areas with SAXS or WAXS scattering present but without well-defined orientation, while white areas correspond to parts without any scattering. Black arrows refer to specific scans across the grain boundaries. c) An optical microscopy image of the same sample. d–m) Average SAXS (d–h) and WAXS (i–m) diffraction patterns with the corresponding peak indexing for each colored domain are shown. The peaks are indexed under the assumption of an fcc structure for the SL and a rock-salt structure of the NCs.

over all diffraction patterns of each of the five domains. The third row (Figure 2k–o) displays the simulated real-space orientations for each domain of the SL based on the geometrical interpretation of the scattering data. The simulated CCFs (blue

dashed curves) in Figure 2a–e are based on the real-space structures shown in Figure 2k–o (see the Supporting Information for details). The good agreement between experimental and simulated CCFs supports the structural interpretation used to index

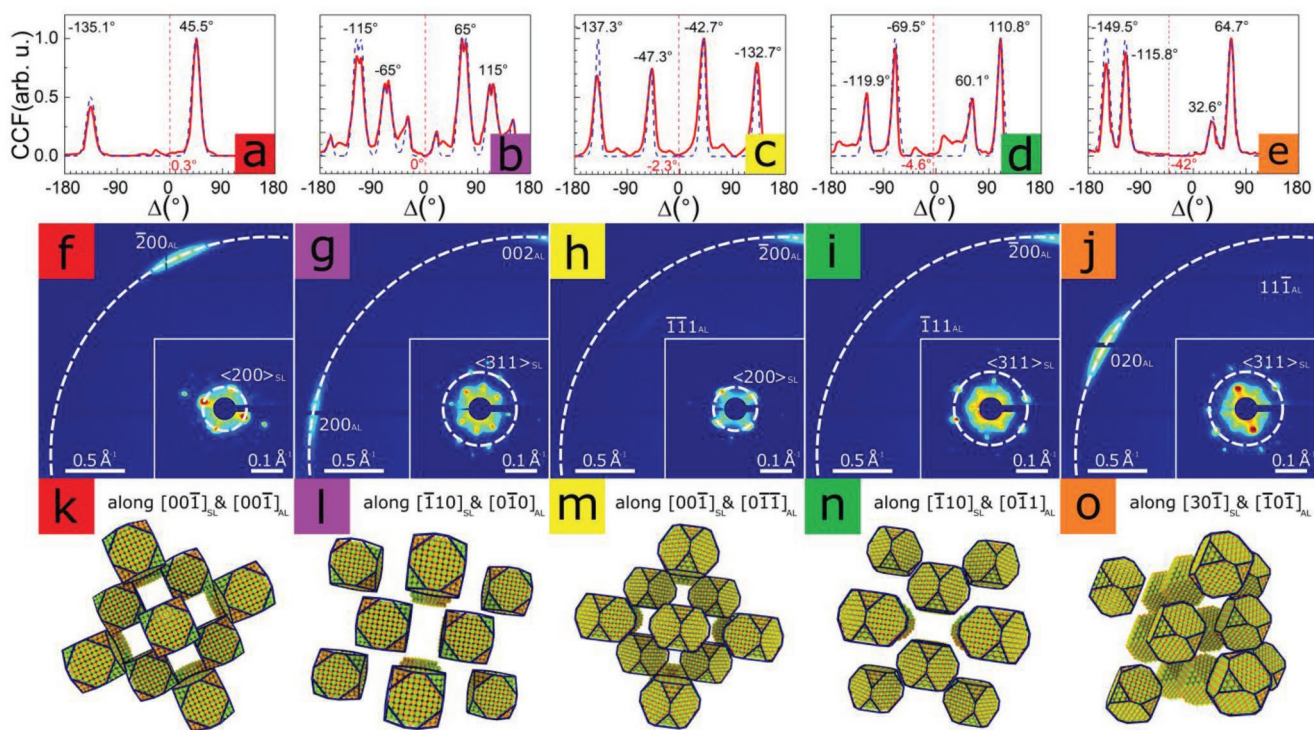


**Figure 2.** a–e) Calculated CCFs (red lines) based on the experimental data and simulated CCFs (blue dashed lines) based on the model structures shown in (k–o), using the  $q$ -values described in the text. f–j) Averaged WAXS diffraction patterns corresponding to each domain. Enlarged SAXS patterns are shown in the lower right corners (note: the center of the WAXS pattern does not coincide with the center of the SAXS pattern due to the different scale). The  $q$ -values used for calculating CCFs are indicated by the white dashed lines. k–o) Real-space models of the superlattice and its constituting NCs based on the SAXS and WAXS patterns and CCFs for all five domains.

Figure 1d–h and serves to understand all further scattering patterns in this work, including individual patterns at grain boundaries. Except for the red and purple domains, we observe four correlation peaks for each domain. For the red domain, there are only two peaks in the CCF due to the low intensity of one pair of SAXS peaks (see Figure 2a). This may be explained by a significant ( $5^\circ$ – $10^\circ$ ) tilt of the SL with respect to the sample surface. However, the relative positions of the SAXS and WAXS peaks in this domain (Figure 2f) are similar to the yellow domain (see Figure 2h). For the purple domain, there are eight peaks in the CCF (Figure 2b) as this domain is characterized by the presence of two  $\langle 200 \rangle_{AL}$  and four  $\langle 311 \rangle_{SL}$  reflections (see Figure 2g). The CCFs for all domains except for the orange one are symmetric with respect to  $\Delta = 0^\circ$ , indicating the symmetry of the angular position of the NCs with respect to the  $\langle 110 \rangle_{SL}$  directions. We have marked the axis of symmetry for the red domain at  $0.3^\circ$  under the assumption that its CCF resembles that of the yellow domain. The axis of symmetry for the orange domain is at  $42^\circ$ , which means that the NCs are not positioned symmetrically in the  $(30\bar{1})_{SL}$  plane. This is further illustrated in Figure 2o by the asymmetric real-space structure in this orientation.

### 2.3. Compression of the Superlattice Near Domain Boundaries

Now, we turn our attention to the study of the SL structure close to domain boundaries. Figure 3a shows variations in the value of the  $q_{200}^{SL}$  momentum transfer within the entire sample. We find

that the average value of  $q_{200}^{SL}$  in the center of each domain far from its boundary is  $0.083 \text{ \AA}^{-1}$  (see Figure S4f–j in the Supporting Information), while near the edge, its value increases up to  $0.10 \text{ \AA}^{-1}$ . This indicates a compression of the superlattice as one approaches the domain boundary. To illustrate this, we select two scans through the boundaries of the purple (scan S1) and orange (scan S2) domains. At each point of the scans, we calculate the positions of the  $\langle 200 \rangle_{SL}$  reflections shown in Figure 3b,c and find an increase of the momentum transfer by 10% and 5%, respectively. We observe the same trend for the peaks of the  $\langle 311 \rangle$  family (see Figure S8 in the Supporting Information). Evidence for a contraction of the superlattice near domain boundaries is also found in a previous report based on electron microscopy (see Figure 1a therein).<sup>[22]</sup>

### 2.4. Rotation of the Superlattice Near Domain Boundaries

In Figure 4, we exemplarily analyze the changes in the orientation of the superlattice and of the NCs near grain boundaries observed along scans S2 and S3 marked in Figure 1a,b. Scan S2 represents the approach from a mesocrystalline domain toward an area without any scattering (orange into white), while scan S3 is an example for a grain boundary between two mesocrystalline domains (green into yellow). In scan S2, the superlattice undergoes an out-of-plane rotation around the  $[010]_{SL}$  axis by  $22^\circ$ , and is simultaneously tilted by  $7^\circ$  (Figure 4a–d), as schematically illustrated in Figure 4e,f. The rotation angles

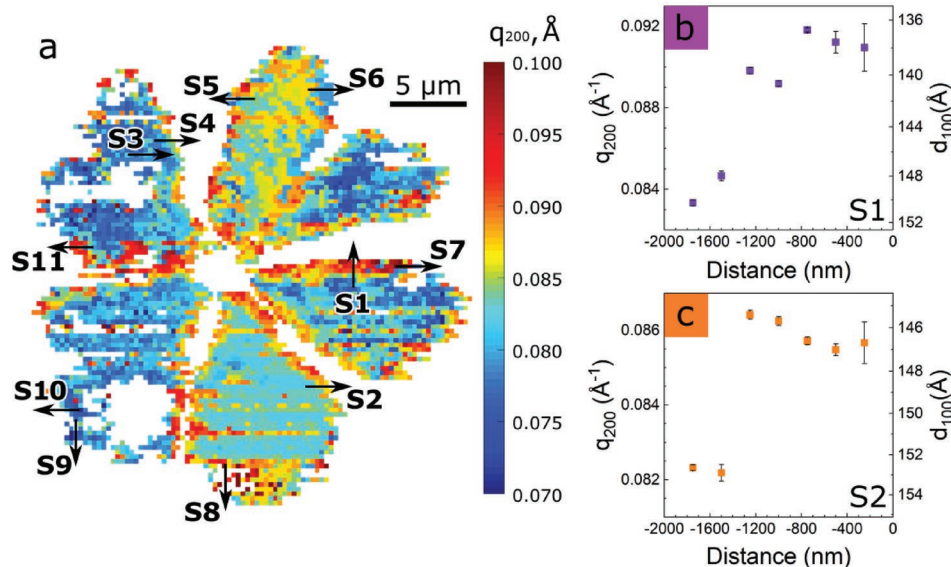


**Figure 3.** a) Spatial map of the momentum transfer value for 200<sub>SL</sub> reflections. The color code quantifies the value of  $q_{200}^{SL}$ . Black arrows refer to specific scans discussed in the text. b, c) Spatial variation in  $q_{200}^{SL}$  between the bulk and the edge of domains for scans S1 (b) and S2 (c).

were obtained by simulation of each individual diffraction pattern from Figure 4a–d (see Figure S11 in the Supporting Information). At the same time, the atomic lattices of all NCs exhibit an out-of-plane rotation around the  $[\bar{1}00]_{AL}$  direction as evidenced by the emerging  $11\bar{1}_{AL}$  Bragg peak (Figure 4b,c, see also Figure S12 in the Supporting Information). The changes in the relative intensities of the  $020_{AL}$  and  $11\bar{1}_{AL}$  peaks indicate the rotation of the AL around the same  $[010]_{SL}$  axis, thus we conclude that the angular correlation is most likely preserved in this example.

In the previous section, we already described the shrinking of the lattice along this scan (see Figure 3c). Therefore, remarkably, although the orientation and lattice spacing of the superlattice change drastically close to the edge of the sample, the angular correlation of the superlattice with the NCs is preserved until the scattering signal vanishes. In scan S3 (Figure 4g–j), the WAXS pattern remains practically unchanged, while the SAXS pattern exhibits a 90° rotation over a distance of 4 μm. This sequence of diffraction patterns can be rationalized as an out-of-plane rotation of both, the SL and AL, around the  $[\bar{1}10]_{SL}$  and  $[001]_{AL}$  axes (which are collinear in the green and yellow domains) by 90°, as detailed in Figure 4k,l. Importantly, the angular correlation between the SL and AL is thus preserved across this grain boundary.

While the SAXS and WAXS patterns of scans S1 and S4–S11 are provided in Figures S9 and S10 (Supporting Information), we note the following general trends: near a grain boundary, the superlattice always experiences an out-of-plane rotation with typical values between 8° and 14°. For the orientation of the NCs, a clear trend is less obvious since the relatively broad Bragg reflections with a full width at half maximum of 15° (see Figure S7 and Table S2 in the Supporting Information) make small out-of-plane rotations difficult to monitor. However, even despite this obstacle, we frequently observe the disappearance of Bragg peaks of the AL while the SL rotates. This indicates either an out-of-plane rotation of the NCs or a

fading scattering signal due to a thin material coverage at the edges of the sample. None of the scans show a pronounced in-plane rotation of the NCs. Thus, the typical grain boundary is characterized by an out-of-plane rotation of the mesocrystalline unit cell by 8°–14°, a compression of the lattice constant by 5–10%, and a preservation of the angular correlation between the superlattice and its constituting NCs. Domains of different angular correlations (e.g., yellow vs red or green vs purple) are separated by extended areas without long-range order of the superlattice and/or no material between these domains.

### 3. Discussion

From the XCCA analysis in Figure 2a–e, we obtain two different angular correlations, which apply to all domains of the sample (Figure 5). In the first configuration (“Conf1,” Figure 5a), we observe the collinearities  $[110]_{SL} \parallel [100]_{AL}$  and  $[001]_{SL} \parallel [001]_{AL}$ . The second configuration (“Conf2,” Figure 5b) is characterized by the collinearities  $[110]_{SL} \parallel [100]_{AL}$  and  $[001]_{SL} \parallel [011]_{AL}$ . We note that a single rotation of all NCs by 45° around the  $[100]_{AL}$  transposes Conf1 into Conf2. While the purple and red domains are characterized by Conf1, the yellow, green, and orange domains are examples for Conf2. To verify this for the orange domain, we simulate the SAXS and WAXS patterns for the superlattice in Figure S3c,h,m (Supporting Information) and find that taking the incident beam directions along the  $[30\bar{1}]_{SL}$  axis reproduces the SAXS pattern of the orange domain as well as the relative scattering intensities of the  $200_{AL}$  and  $111_{AL}$  Bragg peaks. Indicated by the relatively small intensity of the  $111_{AL}$  Bragg peak, the  $[30\bar{1}]_{SL}$  and  $[\bar{1}0\bar{1}]_{AL}$  axes are not exactly collinear, but the difference is negligible when taking into account the calculated misorientation of the NCs (see the Supporting Information). The geometrical relationship between the red and purple domains as well as the yellow, green, and orange domains is indicated with the corresponding colors in Figure 5a,b,

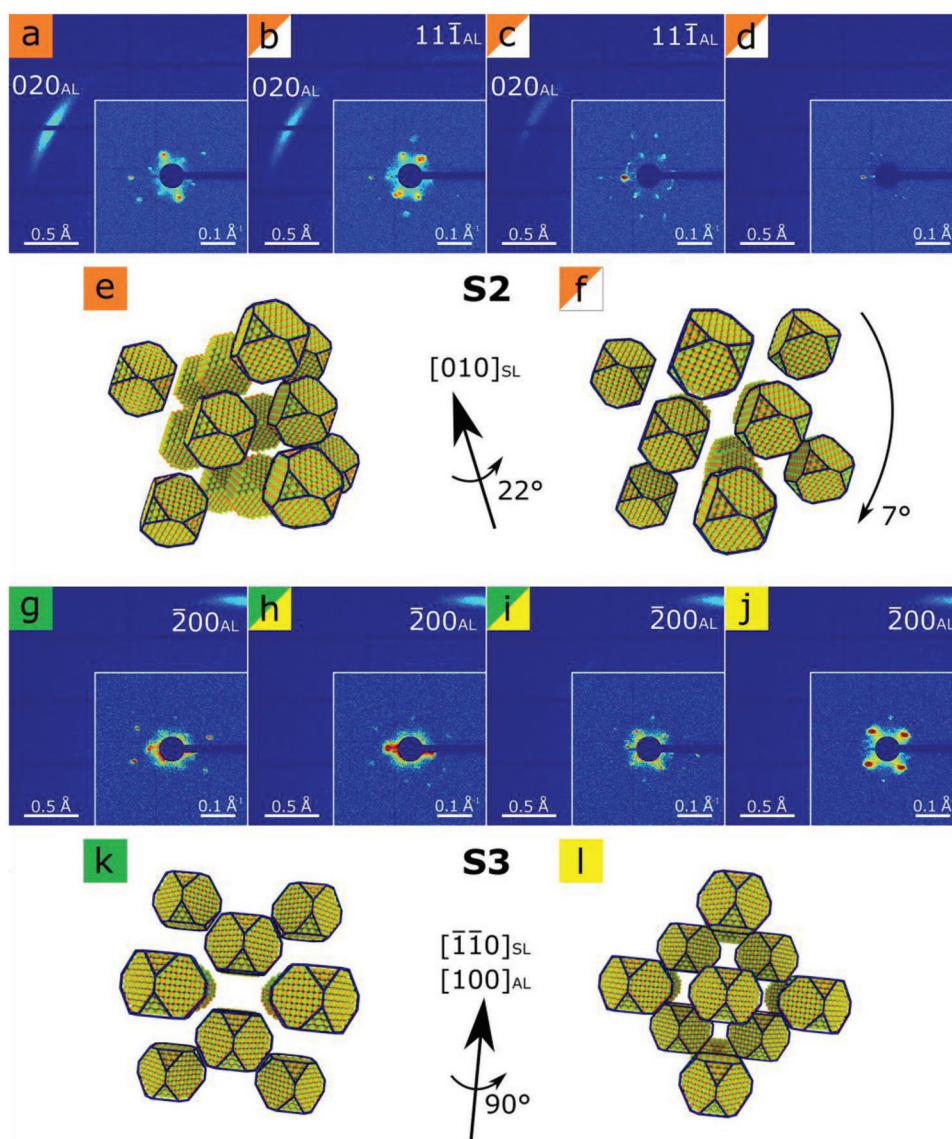


**Figure 4.** a–d) Scan through the border of the purple domain (scan S2 in Figure 1a,b) with 500 nm step size. e,f) The unit cell rotates by  $22^\circ$  around the  $[010]_{\text{SL}}$  direction and is additionally tilted by  $7^\circ$  out-of-plane. g–j) Scan through the border between green and yellow domains of the SL (scan S3 in Figure 1a,b) with  $1 \mu\text{m}$  step size. k,l) The unit cell rotates by  $90^\circ$  around the  $[\bar{1}10]_{\text{SL}}$  and  $[100]_{\text{AL}}$  directions, as indicated in the schematic real-space representations.

respectively. Using an X-ray beam with  $100 \mu\text{m}$  footprint, Li et al. have previously reported diffraction patterns from fcc-PbS NC superlattices exhibiting both configurations Conf1 and Conf2 simultaneously.<sup>[6]</sup> This was attributed to a mixed unit cell of the superlattice consisting of two groups of NCs with the two different angular correlations. By contrast, we exclusively find domains with uniform angular correlation. A possible explanation for these apparently contradicting findings is the much smaller X-ray footprint utilized by us, enabling the analysis of single-crystalline domains of the superlattice. We suggest that the stability of the two configurations is based on the maximization of ligand–ligand interactions between adjacent  $\{100\}_{\text{AL}}$  and  $\{111\}_{\text{AL}}$  facets separated by the nearest-neighbor distance. In a SL with fcc structure, each NC is coordinated 12-fold via

its nearest neighbors along the twelve  $\langle 110 \rangle_{\text{SL}}$  directions. We detail this in Figure 5c,d for both configurations by displaying a  $(1\bar{1}1)_{\text{SL}}$  plane for each, which contain the central NC and six nearest neighbors. If a nearest neighbor directly faces the central NC with a  $\{100\}_{\text{AL}}$  or  $\{111\}_{\text{AL}}$  facet, this is indicated with red and blue ligand molecules, respectively. Otherwise, the ligands between adjacent NCs are omitted for clarity. Conf1 stands out in that all twelve  $\langle 110 \rangle_{\text{SL}}$  directions exhibit such ligand interactions, namely four  $\{100\}_{\text{AL}}-\{100\}_{\text{AL}}$  and eight  $\{111\}_{\text{AL}}-\{111\}_{\text{AL}}$  interactions (see Figure 5c and Figure S13a–c (Supporting Information)). By contrast, Conf2 exhibits only ten such interactions, respectively, all of which occur exclusively between  $\{100\}_{\text{AL}}$  facets (see Figure 5d and Figure S13d–f (Supporting Information)). Since these facets are roughly  $10^6$  times more

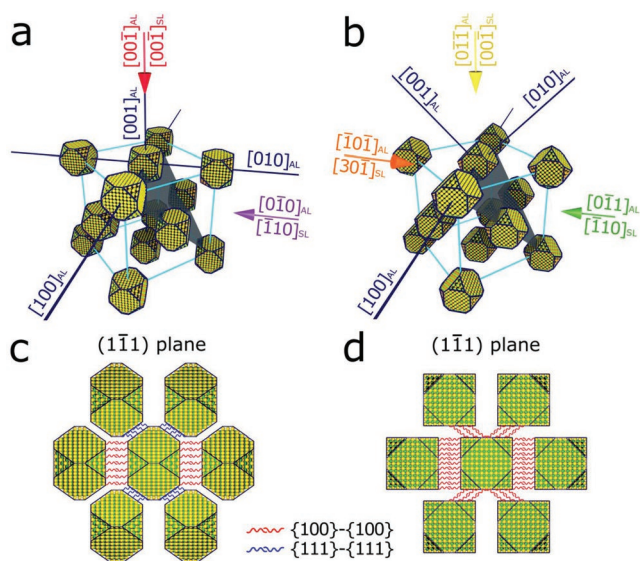


**Figure 5.** a,b) Two different mesocrystalline configurations found in this work. Blue lines show the families of  $\langle 100 \rangle_{\text{AL}}$  directions of the NCs.  $(1\bar{1}\bar{1})_{\text{SL}}$  planes with the highest packing density of the NCs are shown in gray. Colored arrows display the direction of the incoming X-ray beam for each domain corresponding to the diffraction patterns in Figure 1. c,d) View along the  $[0\bar{1}0]_{\text{AL}}$  (c) and  $[0\bar{1}\bar{1}]_{\text{AL}}$  (d) directions of the  $(1\bar{1}\bar{1})_{\text{SL}}$  planes shown in (a) and (b), respectively. In each  $(1\bar{1}\bar{1})_{\text{SL}}$  plane, six nearest-neighbor NCs out of twelve are visible. The facet–facet interaction between central particle and other particles are shown by red ( $\{100\}$ – $\{100\}$  interactions) and blue ( $\{111\}$ – $\{111\}$  interactions) lines.

reactive than  $\{111\}_{\text{AL}}$  facets, we believe that the smaller number of total interactions compared to Conf1 is compensated by the larger number of specific  $\{100\}_{\text{AL}}$ – $\{100\}_{\text{AL}}$  interactions.<sup>[23]</sup>

Recent molecular dynamics simulations have revealed a rich phase diagram for superlattices of NCs depending on the ligand coverage, the particle shape and size, the ligand length, as well as the amount of residual solvent trapped in the superlattice.<sup>[24]</sup> For a partially solvated superlattice, for instance, due to trapped, residual solvent molecules, a truncated octahedral particle shape and a diameter of 6.8 nm, the computed phase diagram predicts the presence of an fcc structure with three distinct angular correlations (“O3-fcc”). We emphasize that the structures observed by us in the present work should be classified as two different types of “UA-fcc,” i.e., a fcc lattice with a uniform angular correlation of all NCs. In this regard, we note that another phase described by Fan and Grünwald (“UA-bct”) is virtually identical to Conf1, apart from a very small tetragonal distortion. Small distortions may be difficult to observe experimentally due to the effect of inhomogeneous shape and size of the NCs. Furthermore, it is noteworthy that for PbS superlattices with fcc structure, polymorphs with only two distinct angular correlations in one domain have been found experimentally.<sup>[6,25]</sup> Similar results were obtained for Si NC superlattices with fcc structure.<sup>[26]</sup> These findings were explained with facet-specific interactions between the substrate and the NCs, directing the NCs into a preferred orientation toward the substrate regardless of the orientation of the superlattice. However, from the five different AL orientations in Figure 1b, only two are characterized by  $\{100\}_{\text{AL}}$ –substrate interactions (red

and purple) and in no case  $\{111\}_{\text{AL}}$  interactions with the substrate are observed. The remaining orientations exhibit interactions between  $\{110\}_{\text{AL}}$  facets and the substrate, but the area of these facets is typically negligible such that the expected interaction energies should be small. It is noteworthy that  $\{100\}_{\text{AL}}$ –substrate interactions are observed only for Conf1 and  $\{110\}_{\text{AL}}$ –substrate interactions only for Conf2. To conclude, the effect of facet–substrate interactions cannot be excluded (in particular for Conf1), but a dominant effect of ligand–ligand interactions is more consistent with our observations in explaining the polymorphism of the fcc structure.

We suggest that facet–substrate interactions play a far more important role in the formation of grain boundaries. Each grain boundary studied by us in Figures 3 and 4 is accompanied by an out-of-plane rotation of the superlattice and a preserved angular correlation with the atomic lattices of the NCs. Thus, the type and number of ligand–ligand interactions does not change in the vicinity of this structural defect, in contrast to the interactions with the substrate. Based on the observation that all grain boundaries are further characterized by a change of the lattice constant (Figure 3), we believe that the predominant driving force for the out-of-plane rotation of the superlattice is the reduction of stress or strain (we note that previous reports have alternatively explained the reduction of the interparticle distance observed near the grain boundaries of a NC superlattice with a reconstruction of the ligand sphere<sup>[27,28]</sup>). A strategy toward mesocrystalline PbS NC superlattices with larger coherent domains should therefore aim at reducing stress/strain in the superlattice – e.g., by a narrower size distribution – as well as maximizing interactions of the NCs with the surface of the substrate to prevent out-of-plane rotations. We anticipate that this may be achieved by coating the substrate with a self-assembled monolayer of a molecular species that interacts strongly with the ligands of the NCs.

## 4. Conclusion

We have identified two distinct mesocrystalline polymorphs of PbS nanocrystal superlattices with face-centered cubic structure, both of which exhibit a rigid iso-orientation of the nanocrystals with the superlattice. We explain this polymorphism with the number of facet-specific ligand–ligand interactions, which are extraordinarily large for both structures. Boundaries between single-crystalline domains occur upon an out-of-plane rotation of the superlattice and the nanocrystals under full preservation of their angular correlation. This out-of-plane rotation is probably caused due to stress or strain in the superlattice as evidenced by a 5–10% compression of the lattice constant during the rotation. We suggest that the key to nanocrystal superlattices with improved long-range order are stronger particle–substrate interactions as the particle–particle interactions are advantageously strong.

## Supporting Information

Supporting Information is available from the Wiley Online Library or from the author.

## Acknowledgements

The authors thank T. Salditt for providing nanofocusing instrument (GINIX) support at the P10 beamline. This work was supported by the DFG under Grant Nos. SCHE1905/3, SCHE1905/4, and SCHR700/25, the Tomsk Polytechnic University Competitiveness Enhancement Program grant (project number VIU-MNOL NK-214/2018) as well as the Helmholtz Association's Initiative and Networking Fund and the Russian Science Foundation Grant No. HRSF-0002.

## Conflict of Interest

The authors declare no conflict of interest.

## Keywords

crystal defects, mesocrystals, nanoparticles, superlattices, X-ray scattering

Received: September 1, 2019

Revised: October 18, 2019

Published online:

- [1] a) M. A. Boles, D. V. Talapin, *J. Am. Chem. Soc.* **2014**, *136*, 5868; b) T. Hanrath, *J. Vac. Sci. Technol., A* **2012**, *30*, 030802; c) M. P. Pileni, P. Davide Cozzoli, N. Pinna, *CrystEngComm* **2014**, *16*, 9365; d) Z. L. Wang, *Adv. Mater.* **1998**, *10*, 13.
- [2] N. Goubet, M. P. Pileni, *J. Phys. Chem. Lett.* **2011**, *2*, 1024.
- [3] K. Bian, J. J. Choi, A. Kaushik, P. Clancy, D.-M. Smilgies, T. Hanrath, *ACS Nano* **2011**, *5*, 2815.
- [4] a) J. J. Choi, C. R. Bealing, K. Bian, K. J. Hughes, W. Zhang, D.-M. Smilgies, R. G. Hennig, J. R. Engstrom, T. Hanrath, *J. Am. Chem. Soc.* **2011**, *133*, 3131; b) B. A. Korgel, S. Fullam, S. Connolly, D. Fitzmaurice, *J. Phys. Chem. B* **1998**, *102*, 8379; c) J. Novak, R. Banerjee, A. Kornowski, M. Jankowski, A. Andre, H. Weller, F. Schreiber, M. Scheele, *ACS Appl. Mater. Interfaces* **2016**, *8*, 22526.
- [5] B. W. Goodfellow, Y. Yu, C. A. Bosoy, D.-M. Smilgies, B. A. Korgel, *J. Phys. Chem. Lett.* **2015**, *6*, 2406.
- [6] R. Li, K. Bian, T. Hanrath, W. A. Bassett, Z. Wang, *J. Am. Chem. Soc.* **2014**, *136*, 12047.
- [7] M. C. Weidman, D.-M. Smilgies, W. A. Tisdale, *Nat. Mater.* **2016**, *15*, 775.
- [8] J. J. Choi, K. Bian, W. J. Baumgardner, D.-M. Smilgies, T. Hanrath, *Nano Lett.* **2012**, *12*, 4791.
- [9] a) A. D. McFarland, M. A. Young, J. A. Dieringer, R. P. van Duyne, *J. Phys. Chem. B* **2005**, *109*, 11279; b) R. Mahadevu, A. Pandey, *J. Phys. Chem. C* **2014**, *118*, 30101; c) B. E. Treml, B. H. Savitzky, A. M. Tirmzi, J. C. DaSilva, L. F. Kourkoutis, T. Hanrath, *ACS Appl. Mater. Interfaces* **2017**, *9*, 13500.
- [10] a) L. Bahrig, S. G. Hickey, A. Eychmüller, *CrystEngComm* **2014**, *16*, 9408; b) H. Cölfen, M. Antonietti, *Angew. Chem., Int. Ed.* **2005**, *44*, 5576; c) R.-Q. Song, H. Cölfen, *Adv. Mater.* **2010**, *22*, 1301.
- [11] I. A. Zaluzhnyy, R. P. Kurta, A. André, O. Y. Gorobtsov, M. Rose, P. Skopintsev, I. Besedin, A. V. Zozulya, M. Sprung, F. Schreiber, I. A. Vartanyants, M. Scheele, *Nano Lett.* **2017**, *17*, 3511.
- [12] M. I. Bodnarchuk, E. V. Shevchenko, D. V. Talapin, *J. Am. Chem. Soc.* **2011**, *133*, 20837.
- [13] a) A. Howie, L. D. Marks, *Philos. Mag. A* **1984**, *49*, 95; b) C. Wang, C. Siu, J. Zhang, J. Fang, *Nano Res.* **2015**, *8*, 2445.
- [14] A. Mayence, D. Wang, G. Salazar-Alvarez, P. Oleynikov, L. Bergstrom, *Nanoscale* **2014**, *6*, 13803.
- [15] a) S. Bao, J. Zhang, Z. Jiang, X. Zhou, Z. Xie, *J. Phys. Chem. Lett.* **2013**, *4*, 3440; b) B. T. Diroll, V. V. T. Doan-Nguyen, M. Cargnello, E. A. Gauding, C. R. Kagan, C. B. Murray, *ACS Nano* **2014**, *8*, 12843; c) S. M. Rupich, E. V. Shevchenko, M. I. Bodnarchuk, B. Lee, D. V. Talapin, *J. Am. Chem. Soc.* **2010**, *132*, 289; d) X. Ye, J. Chen, C. B. Murray, *J. Am. Chem. Soc.* **2011**, *133*, 2613.
- [16] B. T. Diroll, X. Ma, Y. Wu, C. B. Murray, *Nano Lett.* **2017**, *17*, 6501.
- [17] a) B. T. Diroll, N. J. Greybush, C. R. Kagan, C. B. Murray, *Chem. Mater.* **2015**, *27*, 2998; b) S. Disch, E. Wetterskog, R. P. Hermann, D. Korolkov, P. Busch, P. Boesecke, O. Lyon, U. Vainio, G. Salazar-Alvarez, L. Bergstrom, T. Brückel, *Nanoscale* **2013**, *5*, 3969; c) D. K. Smith, B. Goodfellow, D.-M. Smilgies, B. A. Korgel, *J. Am. Chem. Soc.* **2009**, *131*, 3281.
- [18] a) A. Dreyer, A. Feld, A. Kornowski, E. D. Yilmaz, H. Noei, A. Meyer, T. Krekeler, C. Jiao, A. Stierle, V. Abetz, H. Weller, G. A. Schneider, *Nat. Mater.* **2016**, *15*, 522; b) X. W. Gu, X. Ye, D. M. Koshy, S. Vachhani, P. Hosemann, A. P. Alivisatos, *Proc. Natl. Acad. Sci. USA* **2017**, *114*, 2836.
- [19] P. Wochner, C. Gutt, T. Autenrieth, T. Demmer, V. Bugaev, A. D. Ortiz, A. Duri, F. Zontone, G. Grübel, H. Dosch, *Proc. Natl. Acad. Sci. USA* **2009**, *106*, 11511.
- [20] a) M. Altarelli, R. P. Kurta, I. A. Vartanyants, *Phys. Rev. B* **2010**, *82*, 1042017; b) M. Altarelli, R. P. Kurta, I. A. Vartanyants, *Phys. Rev. B* **2012**, *86*, 179904.
- [21] R. P. Kurta, M. Altarelli, I. A. Vartanyants, in *Advances in Chemical Physics* (Eds.: S. A. Rice, A. R. Dinner), John Wiley & Sons, Inc., Hoboken, NJ, USA **2016**, pp. 1–39.
- [22] P. Simon, L. Bahrig, I. A. Baburin, P. Formanek, F. Röder, J. Sickmann, S. G. Hickey, A. Eychmüller, H. Lichte, R. Kniep, E. Rosseeva, *Adv. Mater.* **2014**, *26*, 3042.
- [23] a) M. P. Boneschanscher, W. H. Evers, J. J. Geuchies, T. Altantzis, B. Goris, F. T. Rabouw, S. A. P. van Rossum, H. S. J. van der Zant, L. D. A. Siebbeles, G. van Tendeloo, I. Swart, J. Hilhorst, A. V. Petukhov, S. Bals, D. Vanmaekelbergh, *Science* **2014**, *344*, 1377; b) D. Zherebetsky, M. Scheele, Y. Zhang, N. Bronstein, C. Thompson, D. Britt, M. Salmeron, P. Alivisatos, L.-W. Wang, *Science* **2014**, *344*, 1380; c) M. A. Boles, D. V. Talapin, *Science* **2014**, *344*, 1340.
- [24] Z. Fan, M. Grünwald, *J. Am. Chem. Soc.* **2019**, *141*, 1980.
- [25] P. Simon, E. Rosseeva, I. A. Baburin, L. Liebscher, S. G. Hickey, R. Cardoso-Gil, A. Eychmüller, R. Kniep, W. Carrillo-Cabrera, *Angew. Chem., Int. Ed.* **2012**, *51*, 10776.
- [26] Y. Yu, X. Lu, A. Guillaussier, V. R. Voggu, W. Pineros, M. de La Mata, J. Arbiol, D.-M. Smilgies, T. M. Truskett, B. A. Korgel, *Nano Lett.* **2016**, *16*, 7814.
- [27] M. Boles, D. V. Talapin, *J. Am. Chem. Soc.* **2015**, *137*, 4494.
- [28] P. Schapotschnikow, T. J. H. Vlugta, *J. Chem. Phys.* **2009**, *131*, 124705.